

THE NONLINEAR EVOLUTION OF MASSIVE STELLAR CORE COLLAPSES THAT “FIZZLE”

JAMES N. IMAMURA

Institute of Theoretical Science and Department of Physics, University of Oregon, Eugene, OR 97403

BRIAN K. PICKETT

Department of Chemistry and Physics, Purdue University Calumet, Hammond, IN 46323

AND

RICHARD H. DURISEN

Department of Astronomy, Indiana University, Bloomington, IN 47405

Received 2002 July 17; accepted 2002 December 19

ABSTRACT

Core collapse in a massive rotating star may pause before nuclear density is reached, if the core contains total angular momentum $J \gtrsim 10^{49} \text{ g cm}^2 \text{ s}^{-1}$. In such aborted or “fizzled” collapses, temporary equilibrium objects form that, although rapidly rotating, are secularly and dynamically stable because of the high electron fraction per baryon $Y_e > 0.3$ and the high entropy per baryon $S_b/k \approx 1\text{--}2$ of the core material at neutrino trapping. These fizzled collapses are called “fizzlers.” In the absence of prolonged infall from the surrounding star, the evolution of fizzlers is driven by deleptonization, which causes them to contract and spin up until they either become stable neutron stars or reach the dynamic instability point for barlike modes. The barlike instability case is of current interest because the bars would be sources of gravitational wave (GW) radiation. In this paper, we use linear and nonlinear techniques, including three-dimensional hydrodynamic simulations, to study the behavior of fizzlers that have deleptonized to the point of reaching dynamic bar instability. The simulations show that the GW emission produced by bar-unstable fizzlers has rms strain amplitude $r_{15}h = 10^{-23}$ to 10^{-22} for an observer on the rotation axis, with wave frequency of roughly 60–600 Hz. Here h is the strain and $r_{15} = (r/15 \text{ Mpc})$ is the distance to the fizzler in units of 15 Mpc. If the bars that form by dynamic instability can maintain GW emission at this level for 100 periods or more, they may be detectable by the Laser Interferometer Gravitational-Wave Observatory at the distance of the Virgo Cluster. They would be detectable as burst sources, defined as sources that persist for ~ 10 cycles or less, if they occurred in the Local Group of galaxies. The long-term behavior of the bars is the crucial issue for the detection of fizzler events. The bars present at the end of our simulations are dynamically stable but will evolve on longer timescales because of a variety of effects, such as shock heating, infall, deleptonization, and cooling, as well as gravitational radiation and Newtonian gravitational coupling to surrounding material. Long-term simulations including these effects will be necessary to determine the ultimate fate and GW production of fizzlers with certainty.

Subject headings: gravitational waves — hydrodynamics — instabilities — stars: neutron — stars: rotation — supernovae: general

1. INTRODUCTION

In the *traditional* “fizzler” scenario, core collapse in a massive rotating star is arrested at subnuclear density by the centrifugal force, aborting a prompt supernova event. The further evolution of the collapsed material is supposedly driven by gravitational radiation reaction (GRR) instability of nonaxisymmetric modes that slowly drains angular momentum from the core (e.g., Hayashi, Eriguchi, & Hashimoto 1998, 1999) and causes the fizzler to evolve quasi-statically to neutron star density without a supernova event. This *traditional* fizzler scenario does not envision dynamic instability of barlike modes as a likely alternative. Imamura & Durisen (2001, hereafter Paper I) recently proposed a *modified* fizzler scenario in which dynamic instabilities dominate secular instabilities. Paper I pointed out that the equilibrium fizzlers that form initially from the collapse are dynamically stable to barlike modes because of the high electron per baryon fraction $Y_e (> 0.3)$ and the large entropy per baryon $S_b (\sim 1\text{--}2 k)$ of the core material at neutrino trapping (e.g., Mezzacappa & Bruenn 1993). Paper I further argued that, ignoring infall from the surrounding star, the

subsequent evolution of the fizzled collapse is driven by deleptonization, not by the GRR-driven bar instability. The deleptonizing fizzler contracts and spins up, pushing toward a stable neutron star state or to dynamic barlike instability on a deleptonizing timescale that is between the dynamic and the GRR timescales. Ultimately, a complete understanding of fizzlers requires an understanding of the dynamic barlike instabilities in these hot dense objects and the subsequent behavior of the barlike structures that result from instability.

Observationally, unstable fizzlers have drawn interest recently because they may be detectable sources of gravitational radiation. The idea is not new; collapsing rotating stars were first conjectured to be sources of gravitational radiation in the 1970s (Shapiro & Lightman 1976). Recent investigations have shown that rapidly rotating polytropes, used as models of neutron stars, can produce time-integrated gravitational wave (GW) outputs as large as $10^{-3} M c^2$ (Houser, Centrella, & Smith 1994; Smith, Houser, & Centrella 1996; Houser 1998; New, Centrella, & Tohline 2000). To date, the characteristics of the GW emission produced by bar mode unstable fizzlers with realistic equations

of state (EOSs) have not been determined. Fryer, Holz, & Hughes (2002) recently presented a discussion of the GW emission from a wide range of sources including bar mode unstable proto-neutron stars. Their work on the bar mode was based on detailed axisymmetric core collapse models but used order-of-magnitude estimates to determine the amplitude of the GW emission. Perhaps more important than the integrated power in the GW emission is the GW waveform produced by barlike instabilities. The waveform prediction is uncertain even for polytropic evolutions because of difficulties connected with the modeling of the long-term evolution of barlike instabilities (Pickett, Durisen, & Davis 1996; Smith et al. 1996; Houser 1998; Imamura, Durisen, & Pickett 2000; New et al. 2000; Durisen et al. 2001; Imamura & Durisen 2001). Furthermore, there have only been a few modern general relativistic studies of barlike instabilities in rapidly rotating polytropes and neutron stars (Bonazzola, Friebe, & Gourgoulhon 1996, 1998; Yoshida & Eriguchi 1997, 1999; Stergioulas & Friedman 1998; Shibata, Baumgarte, & Shapiro 2000; Yoshida et al. 2002). Given the potential importance of fizzlers to the current and next generation of GW detectors, more research is needed.

In this paper, we study the nonlinear evolution of dynamic barlike instabilities in fizzlers and calculate their GW luminosities and waveforms by means of three-dimensional hydrodynamic simulations (Pickett et al. 1996) and quasi-linear analysis (Imamura et al. 2000; Imamura & Durisen 2001). We also investigate aspects of deleptonizing fizzlers prior to the onset of full nonlinear dynamic instability by a combination of equilibrium modeling and linear stability analysis techniques (Paper I). The remainder of our paper is organized as follows. In § 2, we discuss the physical picture and modeling of evolving fizzlers. In § 3, we present results of our equilibrium calculations, linear/quasi-linear analyses, and nonlinear simulations of bar mode unstable fizzlers. Section 4 discusses aspects of long-term bar evolution. In § 5, we summarize our principal results and conclusions.

2. PHYSICS AND METHODOLOGY

2.1. Fizzler Formation

Massive stars at the ends of their nuclear lifetimes have iron cores of mass $M_c \approx 1.25\text{--}2.05 M_\odot$ (Timmes, Woosely, & Weaver 1996) with central densities $\rho_c \sim 10^9 \text{ g cm}^{-3}$ and material properties $Y_e \sim 0.4\text{--}0.49$ and $S_b/k \sim 1\text{--}2$ (see Hashimoto 1995). The dynamic collapse of the core is triggered by the deleptonization and cooling of the hot dense material. The core collapse of rotating and nonrotating massive stars shares several common traits; the inner core collapses first while the outer core, to first approximation, remains stationary. The inner core collapses until either nuclear density is reached or it becomes centrifugally supported. In both cases, after the initial collapse, the core rebounds to an equilibrium configuration determined by its mass and angular momentum (Fryer & Heger 2000). A collapse with rotation can overshoot its equilibrium state considerably and then oscillate axisymmetrically about equilibrium (Zwerg & Müller 1997). A fizzler ultimately forms from the collapse if the centrifugal acceleration becomes comparable to the gravitational acceleration at the

core's equator R_{eq} , i.e.,

$$\frac{v^2}{R_{\text{eq}}} \sim \frac{GM_c}{R_{\text{eq}}^2}, \quad (1)$$

at an equilibrium central density ρ_c that is less than nuclear density, $\rho_{\text{nuc}} \approx 1.15 \times 10^{14} \text{ g cm}^{-3}$, defined here by the density ρ , where the Lattimer & Swesty (1991) EOS stiffens. Conservation of angular momentum then leads to the following estimate for the critical angular momentum for fizzler formation,

$$J_f \sim (GM_c^3 R_{\text{eq}})^{1/2} \sim 3 \times 10^{49} \left(\frac{M_c}{1.4 M_\odot} \right)^{3/2} \times \left(\frac{R_{\text{eq}}}{10 \text{ km}} \right)^{1/2} \text{ g cm}^2 \text{ s}^{-1}. \quad (2)$$

2.2. Barlike Instabilities

During collapse and fizzler formation, the hot inner core material maintains a high Y_e (>0.3), and the initial fizzler settles into a state that is stable to both secular and dynamic nonaxisymmetric instabilities due to rotation. For global nonaxisymmetric modes of m -fold symmetry, the most important instabilities in rapidly rotating fizzlers occur for $m = \pm 2$ f -mode surface distortions, which are analogs of the Kelvin bar modes of incompressible fluids (see Chandrasekhar 1969). The *secular* instability is driven by gravitational radiation reaction when an intrinsically retrograde mode is dragged by rotation into prograde motion beyond neutral points along sequences of the rotating equilibrium models. We locate these neutral points using a Lagrangian variational principle (Friedman & Schutz 1978; Imamura et al. 1995), and we calculate the approximate growth times for GRR-driven instabilities by a method described in Paper I. The $m = -2$ barlike mode becomes secularly unstable for a ratio of rotational to gravitational energy $T/|W| > 0.038\text{--}0.14$, the precise value depending on angular momentum distribution, equation of state, and relativistic effects (Stergioulas & Friedman 1998; Toman et al. 1998; Imamura & Durisen 2001). Secular instabilities of higher- m f -modes also occur but with growth times that are much too long to be relevant for fizzlers. The *dynamic* instability sets in when the prograde and retrograde $l = |m| = 2$ f -modes merge and become degenerate at a $T/|W|$ of about 0.27. The dynamic instability threshold can be found by solving the initial value problem for the evolution of linear Eulerian perturbations, as described in Toman et al. (1998) and Paper I. To study the nonlinear development of dynamic instabilities in this paper, we use a version of the nonlinear three-dimensional numerical hydrodynamics code of Pickett et al. (1996). The primary differences between the current numerical code and the Pickett et al. code are that here we consider a barotropic fizzler EOS with fixed Y_e and S/k from Lattimer & Swesty (1991).

After the collapse of the inner core, the outer core accretes onto the inner core on a timescale of 0.01–0.1 s (e.g., see Fryer & Heger 2000). Fizzlers made from cores in the typical core mass range ($1.25\text{--}2.05 M_\odot$) will not be dynamically unstable. This can be seen in Figure 1, where it is apparent that dynamic instability sets in for $M_c > 2 M_\odot$ when $Y_e > 0.3$. Fizzlers may, however, be susceptible to the GRR-driven secular instabilities. Secular instability may set

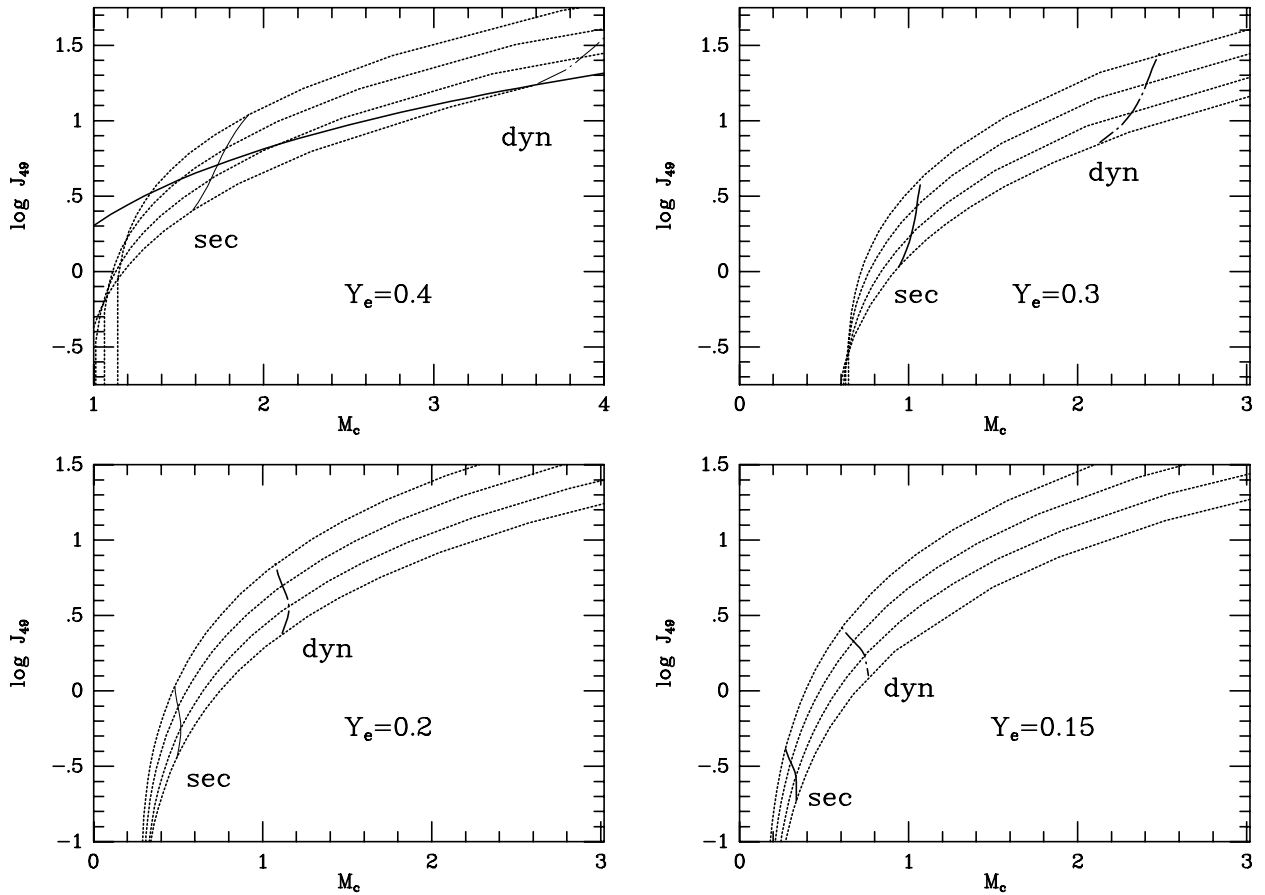


FIG. 1.— M - J relations for fizzlers computed for $K = 180$ MeV, $S_b/k = 1.5$, and $Y_e = 0.4$ (top left), 0.3 (top right), 0.2 (bottom left), and 0.15 (bottom right). The lines are drawn for constant ρ_c . Going from upper left to lower right in each panel, the density curves are for $\rho_c = 10^{11}$, 10^{12} , 10^{13} , and 10^{14} g cm $^{-3}$. The solid lines that cut across the constant ρ_c loci mark the models with $T/|W| = 0.14$, the secular stability limit, and the dot-dashed lines mark $T/|W| = 0.27$, the dynamic stability limit. The unstable models sit to the right of the lines. The heavy bold line in the $Y_e = 0.4$ plot separates the fizzlers that reach $T/|W| = 0.27$ before ρ_{nuc} is reached from those that reach $T/|W| = 0.27$ after ρ_{nuc} is reached; that is, it separates fizzlers into the low- ρ_c and high- ρ_c regimes.

in for $M > 1 M_\odot$ for $Y_e > 0.3$, and fizzlers may become secularly unstable during the accretion of the outer core onto the inner core. Paper I showed, however, that for any Y_e , the GRR timescale τ_{GRR} is too long for secular instability to grow while the fizzler deleptonizes if $\rho_c \lesssim \rho_{\text{nuc}}$. It is only for $\rho_c \gtrsim \rho_{\text{nuc}}$ that τ_{GRR} can be small enough for secular instabilities to grow during deleptonization. However, because $kT \gtrsim 5$ – 10 MeV in this case, bulk viscosity is efficient and will prevent the GRR-driven instability from growing (Lindblom & Detweiler 1977; Yoshida & Eriguchi 1995). Fizzlers are thus neither secularly nor dynamically unstable to nonaxisymmetric modes during and immediately after the early dynamic collapse and accretion phase.

The further evolution is driven by deleptonization. Deleptonization causes a fizzler to contract and spin up, driving it toward rotational instability. Fizzlers deleptonize through neutrino diffusion on roughly the timescale (Burrows, Mazurek, & Lattimer 1981)

$$\langle \tau_{\text{de}} \rangle \approx 0.72 \left(\frac{M}{1.4 M_\odot} \right)^{2/3} \left(\frac{\rho}{10^{13} \text{ g cm}^{-3}} \right) \left(\frac{Y_\nu}{0.1} \right)^{2/3} \times \left(1 + \frac{X_A A}{23.6} \right) \text{ s}. \quad (3)$$

Here $\langle \tau_{\text{de}} \rangle$ includes neutrino-nucleon scattering and

neutrino-nucleon absorption (e.g., Bowers & Deeming 1984). In the above, Y_ν is the neutrino fraction per baryon, X_A is the mass fraction for nuclear species A , A is the nuclear mass, and we replaced ρ with $(3M/4\pi R_{\text{eq}}^3)$. For $\langle \tau_{\text{de}} \rangle$ it is assumed that the baryon number density is constant and that the lepton fraction per baryon Y_l is equal to the neutrino fraction per baryon Y_ν . Later, we find more precise deleptonization timescales by solving the neutrino transport equation in the diffusion approximation (Burrows et al. 1981). For this section, we need only rough timescales. A $1.4 M_\odot$ fizzler with $\rho_c = \rho_{\text{nuc}}$ is beyond the nucleon-nuclei transition, and so the opacity is dominated by neutrino-nucleon scattering and $\langle \tau_{\text{de}} \rangle \sim 14(Y_\nu/0.1)^{2/3}$ s. For smaller ρ_c , the opacity is dominated by coherent absorption on nuclei and $\langle \tau_{\text{de}} \rangle \approx 3(\rho X_A/10^{13} \text{ g cm}^{-3})(A/100)(Y_\nu/0.1)^{2/3}$ s.

The first instability encountered by a fizzler that is fast enough to grow during deleptonization is the dynamic barlike mode instability. The barlike instability leads to the formation of a central bar surrounded by expanding spiral arms, as first shown for polytropes by Durisen et al. (1986). Such instabilities break the axisymmetry of the fizzler with interesting observational consequences. For us, the most interesting one is that the time-dependent nonaxisymmetric form leads to GW production, making fizzlers relevant to the Laser Interferometer Gravitational-Wave Observatory

(LIGO) and the other GW detectors currently coming on-line. We consider the details of the GW emission in this paper.

2.3. Onset of Barlike Instabilities

When and how dynamic instability occurs in a deleptonizing fizzler is a matter of some debate. The physical issue is identical to that which arises in the discussion of the fission theory for binary star formation (e.g., see Tassoul 1978; Durisen & Tohline 1985; Tohline & Durisen 2001). For binary star formation in inviscid fluids, Tassoul delineates two scenarios:

1. *The Lebovitz approach.*—Lebovitz (1972) argued that cooling contracting protostars that are rotating will unavoidably have some degree of nonaxisymmetry. Even if the nonaxisymmetry is initially small, a cooling protostar will contract along a triaxial sequence rather than along an axisymmetric one. Thus, the protostar avoids the dynamic bar mode instability. It instead contracts along the triaxial sequence until it encounters a higher-order bifurcation into a third- or fourth-order surface distortion. The higher-order surface distortion is conjectured to lead to fission and the formation of a binary star system.

2. *The Ostriker approach.*—Ostriker argued instead that a cooling contracting protostar remains essentially axisymmetric as it evolves and so encounters the dynamic barlike mode instability. The evolution then becomes dynamic and perhaps even catastrophic. To date, all careful calculations that have followed slow evolution to the dynamic bar instability, usually through accretion (e.g., Bate 1998), have supported the Ostriker scenario.

This paper assumes that the second approach is correct. We are currently conducting a study of deleptonizing fizzlers and cooling polytropes to study the problem. Our preliminary result is that as long as nonaxisymmetry in the polytrope is *linear* in amplitude at the time the dynamic barlike mode instability threshold is crossed, the evolution is not much different from one that starts with a finitely unstable axisymmetric model. No high-order bifurcations seem to manifest themselves. Because of the importance of this issue, we plan to study it in greater depth and will report the details elsewhere. To determine whether the nonaxisymmetric modes will remain small prior to the onset of dynamic instability for fizzlers will require detailed numerical core collapse calculations with rotation in three dimensions. There have been few such attempts (e.g., Rampp, Müller, & Ruffert 1998), and they do not shed much light on this issue.

2.4. *r*-Mode Instabilities

It has been shown recently that nonaxisymmetric *r*-modes can also be secularly unstable due to GRR (Andersson 1998; Friedman & Morsink 1998). The mechanism is similar to secular instability of *f*-modes in that it occurs when retrograde modes are dragged into prograde motion by stellar rotation. The GW emission by *r*-mode instabilities is dominated by mass currents rather than by the time-dependent spatial mass distortions that prevail for *f*-modes. There are no dynamic instabilities known for *r*-modes in neutron stars, and, even at neutron star densities with fast rotation, the τ_{GRR} for the fastest growing $l = m = 2$ *r*-mode is relatively long, ~ 40 s (Lindblom, Owen, & Morsink 1998). The growth times vary roughly as R_{eq}^8 for $l = 2$ when M and J

are held fixed, and so τ_{GRR} will be orders of magnitude longer in the fizzler regime. In fact, the τ_{GRR} values for the *r*-modes are very much longer than those for the barlike modes, which were shown in Paper I to be ~ 10 s for models with $\rho_c \approx \rho_{\text{nuc}}$ at the high-density end of the fizzler regime. As pointed out in Paper I and § 2.2 above, the deleptonization times for fizzlers tend to be ~ 1 – 10 s. The *r*-modes are thus of no consequence for fizzler evolution. They are, however, likely to be important for lowering the initial spin rates of young, hot neutron stars over a timescale on the order of a year (Lindblom et al. 1998; Stergioulas & Font 2001; Lindblom, Tohline, & Vallisneri 2001). The *r*-modes are more important than *f*-modes in this context, because there are unstable $l = 2$ *r*-modes for all Ω , while the $m = 2$ *f*-mode GRR instability occurs only for relatively large values of $T/|W| \sim 0.14$. Modes with higher l are much less efficient radiators.

2.5. Gravitational Radiation

The GW strains and torques are calculated using the quadrupole approximation in the Newtonian limit (e.g., see Finn & Evans 1990). The strain induced by the gravitational radiation is represented as

$$g_{\mu\nu} = \eta_{\mu\nu} + h_{\mu\nu}, \quad (4)$$

where $g_{\mu\nu}$ is the metric tensor, $\eta_{\mu\nu}$ is the Minkowski metric, and $h_{\mu\nu}$ is the strain tensor, where $|h_{\mu\nu}| \ll |\eta_{\mu\nu}|$. The strains for the two GW polarization modes are

$$h_+ = \frac{G}{rc^4} \left(\frac{\partial^2 I_{xx}}{\partial t^2} \cos^2 \theta + \frac{\partial^2 I_{zz}}{\partial t^2} \sin^2 \theta - \frac{\partial^2 I_{xz}}{\partial t^2} \sin 2\theta - \frac{\partial^2 I_{yy}}{\partial t^2} \right) \quad (5)$$

and

$$h_\times = \frac{2G}{rc^4} \left(\frac{\partial^2 I_{xy}}{\partial t^2} \cos \theta - \frac{\partial^2 I_{yz}}{\partial t^2} \sin \theta \right), \quad (6)$$

where I_{ij} is the quadrupole moment tensor,

$$I_{ij} = \int \rho \left(x'_i x'_j - \frac{1}{3} \delta_{ij} r'^2 \right) d^3x, \quad (7)$$

and r and θ are the usual spherical coordinates, where θ is measured from the rotation axis. The GRR torque is

$$\dot{J}_i = \frac{2G}{5c^5} \epsilon_{ijk} \left\langle \frac{\partial^2 I_{jm}}{\partial t^2} \frac{\partial^3 I_{km}}{\partial t^3} \right\rangle. \quad (8)$$

We follow New et al. (2000) in our implementation of the GW formalism.

3. FIZZLER EVOLUTION RESULTS

In this section, we investigate the evolution of post-collapse fizzlers after their accretion phase and ignore possible effects of any residual infall. In § 3.1, we follow the quasi-static contraction due to deleptonization up to dynamic bar instability in an approximate way, by constructing sequences of equilibrium models. The onset and nonlinear evolution of the dynamic barlike mode instability is then treated in § 3.2 for a few particular cases by using our unique combination of linear, quasi-linear, and nonlinear techniques.

3.1. Deleptonization

The quasi-static contraction of fizzlers due to deleptonization can be mimicked by constructing sequences of axisymmetric equilibrium models with the same mass M_c , angular momentum J_c , and angular momentum distribution, but with decreasing Y_e . We use the hot EOS of Lattimer & Swesty (1991) and the Maclaurin spheroid specific angular momentum distribution (see Paper I). Hayashi et al. (1998) and Paper I found that Y_e has the greatest effect on fizzler properties, so here we consider only the decrease in Y_e due to deleptonization and keep S_b constant. For a given S_b , Y_e , and nuclear matter compressibility (here set at 180 MeV; see Hayashi et al. 1998, 1999), we may define a barotropic EOS suitable for the Hachisu-style (Hachisu 1986) self-consistent-field two-dimensional equilibrium model code described in Paper I. The assumption of constant Y_e and S_b throughout the body of a fizzler at given time is clearly an approximation, but it does capture the important global effects (Strobel, Schaab, & Weigel 1999).

Figure 1 illustrates the effect of deleptonization on fizzlers in (M_c, J_c) -space by plotting loci of constant ρ_c for four values of Y_e . These curves are from differentially rotating fizzler models with an angular momentum distribution identical to that of the Maclaurin spheroids (the $n' = 0$ distribution of Paper I). The highest density sequence shown in Figure 1 for a given Y_e , namely, $\rho_c = 10^{14}$ g cm $^{-3}$, roughly divides the parameter space for the given EOS into regions of direct collapse to neutron star densities in the lower right and fizzler formation to the upper left. We estimate the thresholds for fizzler formation as follows. At neutrino trapping, the lepton fraction is roughly $Y_l \approx 0.4$ –0.45 and $Y_e \approx 0.32$ –0.35 (e.g., Mezzacappa & Bruenn 1993). Using the $Y_e = 0.3$ and 0.4 plots to bound the range of values for the fizzler formation thresholds, we find $J_f \sim (2$ – $1) \times 10^{49}$ g cm 2 s $^{-1}$, $(3.5$ – $2) \times 10^{49}$ g cm 2 s $^{-1}$, and $(6$ – $5) \times 10^{49}$ g cm 2 s $^{-1}$ for $Y_e = 0.3$ –0.4 for the masses $M_c = 1.2$, 1.6, and 2 M_\odot , respectively. The specific angular momenta (J_f/M_c) are similar to the specific angular momenta for the iron cores of massive rotating stars found by Heger, Langer, & Woosley (2000) in detailed calculations of the evolution of rapidly rotating massive stars. Recent hydrodynamic models of convective cores in rapidly rotating stars (Deupree 2001) indicate that they are differentially rotating. The assumption used by Heger, Langer, & Woosley of uniform rotation in convective regions underestimates the core

angular momentum and leads to specific angular momentum distributions that concentrate more angular momentum toward the equatorial regions of the core than for cores with differential rotation. The latter has a strong effect on the structures and stability properties of the resultant fizzlers (Imamura & Durisen 2001); as discussed in § 4.3, for a given M_c and J_c , the angular momentum distribution can make the difference between formation of a fizzler or a neutron star.

The solid lines in Figure 1 mark the bar mode secular stability limits, and the dot-dashed lines mark the barlike mode dynamic stability limits. The stability limits depend strongly on Y_e . The GRR-driven secular stability limit of the bar modes drops from 1.6–1.9 M_\odot for $Y_e = 0.4$ to 0.25–0.32 M_\odot for $Y_e = 0.15$. The dynamic stability limit drops from 3.7–4.5 to 0.6–0.75 M_\odot for the same change in Y_e . For typical core masses $M_c \sim 1.2$ –2 M_\odot , fizzlers first become dynamically unstable when Y_e reaches 0.2–0.3 depending on M_c . The bold line on the $Y_e = 0.4$ panel in Figure 1 separates those fizzlers that reach $T/|W| = 0.27$ before nuclear density is reached (*above the line*) from those that reach $T/|W| = 0.27$ after nuclear density is reached (*below the line*). We refer to fizzlers that reach dynamic instability with $\rho_c < \rho_{\text{nuc}}$ as “low- ρ ” fizzlers and those that reach instability with $\rho_c > \rho_{\text{nuc}}$ as “high- ρ ” fizzlers.

The precipitous decline in the masses of the stability limits as Y_e decreases can easily be understood from an examination of the deleptonization sequences in Table 1. Because our equilibrium code keys on ρ_c and degree of flattening, as discussed in Paper I, these sequences had to be interpolated among a large set of models. This was done carefully enough to guarantee that all models in the sequence have the same M_c and J_c to within about a percent or less. The τ_c in Table 1 is the central rotation period of the fizzler. The τ_{de} are the longest local deleptonization timescales found in each model. The τ_{de} are defined as $Y_l/|\dot{Y}_l|$, where the run of \dot{Y}_l in each model is determined by solving the neutrino transport equation in the diffusion approximation. The τ_{de} for the lower angular momentum fizzler with $Y_e = 0.3$ is not given because of numerical difficulties with models that have ρ_c near ρ_{nuc} . This is also the reason why ρ_c is not monotonic for the last three entries. Table 1 shows that, as deleptonization weakens the pressure support, the fizzlers contract quasi-statically to higher densities, with a consequent shortening of the dynamic timescales. Because the angular momentum is conserved during the contraction, the fizzlers

TABLE 1
DELEPTONIZING FIZZLER SEQUENCES

M_c (M_\odot)	J_c (g cm 2 s $^{-1}$)	Y_e	$T/ W $	ρ_c (g cm $^{-3}$)	R_{eq} (km)	τ_c (ms)	τ_{de} (s)
1.58.....	4.97×10^{49}	0.40	0.110	5.79×10^{11}	539.8	34.1	0.0092
		0.30	0.220	1.24×10^{13}	225.5	6.32	0.13
		0.25	0.265	3.03×10^{13}	183.6	4.04	0.23
		0.23	0.285	5.62×10^{13}	159.0	2.98	0.48
		0.20	0.309	8.73×10^{13}	144.2	2.42	0.61
1.60.....	3.29×10^{49}	0.40	0.132	1.79×10^{13}	175.1	5.81	0.28
		0.30	0.225	1.40×10^{14}	76.4	1.79	...
		0.25	0.276	2.48×10^{14}	70.2	1.36	5.9
		0.20	0.279	2.18×10^{14}	62.0	1.46	2.8
		0.15	0.285	2.24×10^{14}	44.1	1.45	13

TABLE 2
EQUILIBRIUM FIZZLERS

Model	Y_e	M_c (M_\odot)	$T/ W $	ρ_c (g cm^{-3})	J_c ($\text{g cm}^2 \text{s}^{-1}$)	R_{eq} (km)	τ_c (ms)
1a.....	0.24	1.37	0.255	10^{13}	4.68×10^{49}	241	7.01
1b.....	0.23	1.58	0.285	5.62×10^{13}	4.97×10^{49}	159	2.98
1c.....	0.23	1.25	0.260	1.26×10^{14}	2.75×10^{49}	110	1.99
2a.....	0.15	1.60	0.285	2.24×10^{14}	3.29×10^{49}	44.1	1.45
2b.....	0.15	1.42	0.271	2.25×10^{14}	2.59×10^{49}	46.6	1.43
2c.....	0.15	1.78	0.268	2.65×10^{14}	3.62×10^{49}	42.7	1.38

spin up and flatten so that $T/|W|$ increases rapidly. This is equivalent to the drop in the masses for the stability limits in Figure 1.

Table 2 shows possible endpoints of a selection of fizzler deleptonization sequences. The entries are given in order of increasing ρ_c . These models are all beyond the dynamic stability limit, which, as shown in Paper I, occurs at roughly $T/|W| \approx 0.26$ for $\rho_c < \rho_{\text{nuc}}$ and $T/|W| \approx 0.27$ for $\rho_c > \rho_{\text{nuc}}$. Models 1b and 2a are from the sequences given in Table 1.

3.2. Dynamic Evolution

In this section, we consider the behavior of fizzlers that have become dynamically unstable to the barlike modes. Table 2 contains the models we have chosen for detailed study. Some results for all six unstable fizzlers are quoted in Tables 2–4 based on application of our linear and quasi-linear methods. The barlike instabilities for two of the fizzlers (models 1b and 2a in Table 2) have been followed using our nonlinear three-dimensional hydrodynamics code.

3.2.1. Linear Results

Table 3 gives barlike mode oscillation periods P_2 and dynamic e -folding times τ_g as determined by the linear analysis techniques of Paper I. The waveform produced by a tumbling bar will have a single wave cycle in the period P_2 . So when they become dynamically unstable to the barlike modes, fizzlers will emit radiation with periods of ~ 1.7 – 16 ms or frequencies of 60–600 Hz. The τ_g in Table 3 vary considerably because models 1a and 2c were chosen to be just beyond the dynamic instability threshold. Arbitrarily close to the threshold, the growth time becomes infinite. However, the other four models show that one does not have to exceed the threshold by a large amount in $T/|W|$ before the growth times become comparable to the dynamic timescale as measured by the central rotation period τ_c . Then the barlike modes grow fast relative to the timescale for further

deleptonization, and we can evolve these models far into the nonlinear regime with an explicit hydrodynamics code without including deleptonization. The typical structure of the dynamically unstable models is illustrated in Figures 2 and 7, for models 2a and 1b, respectively.

3.2.2. Quasi-linear Results

As first established by Tohline, Durisen, & McCollough (1985), the barlike mode eigenfunctions for differentially rotating compressible fluids have a spiral character with a central coherent bar and outer trailing spiral arms. As this pattern grows to nonlinear amplitude, Newtonian gravitational torques transfer angular momentum from the central bar to the outer arms (Durisen et al. 1986). The material in the spiral arms then expands to form a ring or disk around the bar. As shown in Imamura et al. (2000), it is possible to predict many aspects of the nonlinear behavior from a quasi-linear approach. Let $\rho_0(\varpi, z)$ and $\Omega(\varpi)$ be the axisymmetric equilibrium density and fluid rotation rate, $\delta_{j\phi}$ the δ -function, and $\rho_1(\varpi, z)$ and $v_{j,1}(\varpi, z)$ the density and velocity eigenfunctions for the unstable barlike mode. Then, the density given by

$$\rho(\varpi, \phi, z) = \rho_0(\varpi, z) + \text{Re}[\rho_1(\varpi, z) \exp(2i\phi)] \quad (9)$$

and the velocity field in the bar frame given by

$$v_j(\varpi, \phi, z) = \left[\Omega(\varpi) - \frac{2\pi}{P_2} \right] \varpi \delta_{j\phi} + \text{Re}[v_{j,1}(\varpi, z) \exp(2i\phi)] \quad (10)$$

approximate the structure of a core with a finite amplitude barlike mode perturbation (see Paper I, Fig. 5). When the eigenfunction amplitudes are normalized to the global perturbation amplitude

$$\delta\mathcal{M} = \frac{\int |\rho_1(\varpi, z)| d^3x}{M_c}, \quad (11)$$

TABLE 3
BAR PROPERTIES: QUASI-LINEAR RESULTS

Model	M_b/M_c	R_b (km)	J_b ($\text{g cm}^2 \text{s}^{-1}$)	\dot{J}_b $\text{g cm}^2 \text{s}^{-2}$	\dot{J}_{GW}/\dot{J}_b	$\delta\mathcal{M}/\mathcal{A}_2$	P_2 (ms)	τ_g (ms)
1a.....	0.94	96.6	3.58×10^{49}	4.77×10^{49}	0.00449	1.02	16.2	381
1b.....	0.76	51.7	2.68×10^{49}	3.58×10^{50}	0.00154	1.17	5.78	7.36
1c.....	0.86	43.7	1.10×10^{49}	1.74×10^{50}	0.00252	1.08	4.86	13.1
2a.....	0.90	26.6	2.57×10^{49}	8.21×10^{50}	0.0259	1.02	1.82	1.28
2b.....	0.91	24.1	2.05×10^{49}	2.33×10^{50}	0.0584	1.00	1.85	3.48
2c.....	0.93	24.9	3.05×10^{49}	1.36×10^{50}	0.160	1.00	1.73	79.8

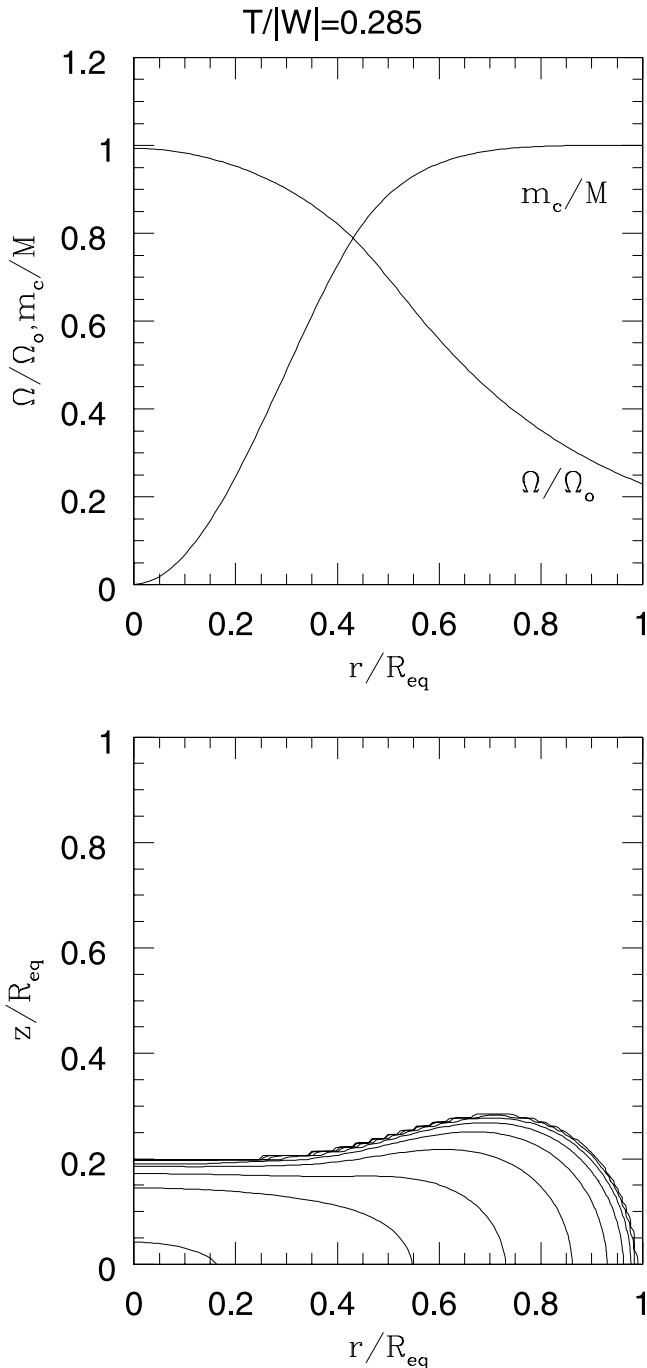


FIG. 2.—Equilibrium density structure and $\Omega(\varpi)$ and $m_c(\varpi)$ distributions for a $1.60 M_\odot$ fizzler calculated for the specific angular momentum distribution of a Maclaurin spheroid and EOS parameters $Y_e = 0.15$, $S_b = 1.5$ k, and $K = 180$ MeV. The model is just beyond the dynamic stability limit with $\rho_c = 2.24 \times 10^{14}$ g cm $^{-3}$, $J = 3.29 \times 10^{49}$ g cm 2 s $^{-1}$, and $T/|W| = 0.285$. The contour levels are set to $\rho/\rho_c = 0.9, 0.1, 0.01, 0.001, 10^{-4}, 10^{-5}, 10^{-6}$, and 10^{-7} . The fizzler has a central $\Omega_0 = 3433$ rad s $^{-1}$.

from the nonlinear simulation, the structures produced in this manner are quite similar in appearance to those found in our nonlinear simulations, and the Newtonian self-interaction torques based on the quasi-linear structures are in quantitative agreement with those found in nonlinear simulations (Imamura et al. 2000; Imamura & Durisen 2001).

Table 3 summarizes some of the quasi-linear properties of the dynamic instabilities for the fizzlers listed in Table 2.

The first column gives M_b , the mass of the bar, determined by the cylindrical radius where the Newtonian torques change sign from negative to positive near the end of the central bar. Experience shows that this is an excellent predictor of the mass of the central, angular momentum–losing bar. The bar radius R_b and angular momentum J_b are computed similarly. The Newtonian torque on the bar \dot{J}_b and the GRR torque on the whole configuration \dot{J}_{GW} are computed assuming that the peak $\delta\mathcal{M} = 1$. The torques scale as $\delta\mathcal{M}^2$. The peak GW strain amplitudes for the viewing angles $\theta = 0^\circ, 45^\circ$, and 90° are given in Table 4. The strains are also calculated for $\delta\mathcal{M} = 1$. The strains scale as $\delta\mathcal{M}$. The rms h , \dot{J}_b , and \dot{J}_{GW} values are $2^{-1/2}$ of the values given in Tables 3 and 4. Note that the wave frequencies and strains are factors of 3–10 higher for high- ρ fizzlers than for low- ρ fizzlers. The amplitudes of both polarizations are the same due to symmetry when the fizzler is viewed down the rotation axis. The strain h_+ , which is aligned with the symmetry axes, decreases in amplitude by only a factor of about 2 as $\theta \rightarrow 90^\circ$, but h_\times decreases by a factor of more like 5–8. A similar decrease in the amplitude of h_+ as $\theta \rightarrow 90^\circ$ is shown in Figure 16 of Houser (1998) for $n = 0.5$ polytropes, meant to mimic the stiff EOS of neutron stars. Evidently, the θ -dependence of GW emission by barlike modes is not sensitive to the EOS.

3.2.3. Nonlinear Simulation of a High- ρ Fizzler

Here we report results from the dynamic evolution of the $1.60 M_\odot$ fizzler with $J = 3.29 \times 10^{49}$ g cm 2 s $^{-1}$ (model 2a) using our nonlinear three-dimensional hydrodynamics code. As can be seen from the bottom sequence of Table 1, for $Y_e \approx 0.32$, this fizzler initially has ρ_c on the order of ρ_{nuc} and $T/|W|$ greater than the bar mode secular stability limit, but smaller than the bar mode dynamic stability limit. The τ_{de} is probably on the order of seconds, and so the fizzler contracts slowly and spins up to dynamic instability. The deleptonized unstable fizzler chosen for numerical simulation has $(Y_e, S_b/k) = (0.15, 1.5)$ and is the last model in the bottom sequence of Table 1. For this Y_e , $\rho_c > \rho_{\text{nuc}}$, and $T/|W| = 0.285$, about 6% beyond the dynamic stability limit $|W| \approx 0.27$. The properties of the deleptonized equilibrium fizzler are given in Table 2 and its structure shown in Figure 2. We use our linear analysis to test low-order m -values. For model 2a, we find only the $m = 2$ barlike mode to be unstable. The oscillation period P_2 is 1.82 ms, and the growth time τ_g is 1.28 ms.

Our three-dimensional hydrodynamics code is explicit, Eulerian, and fully second-order. The equations of hydrodynamics and Poisson’s equation are solved on a static,

TABLE 4
GRAVITATIONAL WAVE EMISSION: LINEAR RESULTS

Model	Frequency (Hz)	$r_{15}h_+/10^{-23\text{a}}$	$r_{15}h_\times/10^{-23\text{a}}$
1a.....	61.7	1.78, 1.50, 0.890	1.78, 1.49, 0.325
1b.....	173	5.43, 4.50, 2.71	5.43, 4.45, 0.863
1c.....	206	4.44, 3.73, 2.22	4.44, 3.71, 0.802
2a.....	549	18.8, 15.3, 9.39	18.8, 15.0, 2.34
2b.....	540	15.2, 12.4, 7.60	15.2, 12.2, 2.06
2c.....	578	21.5, 17.6, 10.7	21.5, 17.2, 2.89

^a The three entries are for the viewing angles $\theta = 0^\circ, 45^\circ$, and 90° , respectively.

uniform, cylindrical grid (Pickett et al. 1996). Simulation begin with a low-level, cell-to-cell random density perturbation $\delta\rho$, such that $-0.005 < \delta\rho/\rho < 0.005$. The low- ρ and high- ρ models are evolved over 70,000 and 80,000 computation steps, respectively, or about 20 central initial rotation periods. The initial grid size is $(r, \varphi, z) = (128, 64, 32)$. Since the models expand significantly in the radial and vertical directions during the course of the simulations, the computational grids are increased to $(r, \varphi, z) = (512, 64, 128)$. Material loss from the expanded grids is rather small and only measurable in the high- ρ case; roughly 0.5% of the total angular momentum and 0.1% of the total mass escape the grid by the end of the run. Weak shocks form in these calculations when material falls back from the ejected spiral arms. In the code version used for these fizzler calculations, entropy generation in the shocks is ignored because S/k is treated as a constant in the EOS. This should lead to some nonconservation of energy. However, the degenerate constituents of the gas contribute most to the EOS; and so, despite the presence of weak shocks, energy is conserved to better than 0.1% throughout both the high- ρ and low- ρ fizzler simulations.

Figures 3–5 demonstrate that the nonlinear evolution of the dynamically unstable barlike mode in the high- ρ fizzler is qualitatively similar to that reported for polytropes since the mid-1980s (e.g., Durisen et al. 1986; Imamura et al. 2000). Figure 3 shows the low-order global Fourier amplitudes for the nonaxisymmetric density perturbations. The Fourier amplitudes \mathcal{A}_m are related to, but are not identical with, the $\delta\mathcal{M}$ defined for the linear analysis (see Imamura et al. 2000). For model 2a, $\delta\mathcal{M} = 1.02 \mathcal{A}_2$ based on the linear results (Table 3). Figure 4 presents gray-scale images of the fizzler density structure in the equatorial plane at various times, and Figure 5 shows two equal density surfaces for the final times in the evolution.

The bar mode self-organizes out of random imposed noise by time $t \approx 0.004\text{--}0.005$ s $\approx 1\text{--}1.5$ pattern periods, where the pattern period $P_p = 2P_2 \approx 0.0036$ s. Once estab-

lished, the barlike mode grows exponentially. As \mathcal{A}_2 approaches its peak amplitude, illustrated by the $t = 0.0173$ s model in Figure 4, the fizzler develops strong material spiral arms. Newtonian torques cause the central bar to shed angular momentum to the outer spiral arms, ending the linear growth phase. As shown in Figure 3, the peak amplitude at saturation is $\mathcal{A}_2 = 0.69$ ($\delta\mathcal{M} \approx 0.70$). The high-order even- m Fourier components at this time are not independent modes but are harmonics of the nonlinear bar mode structure. As the spiral arms expand and wrap, the bar relaxes back to lower amplitude and then rebounds modestly, as shown by the local minimum in \mathcal{A}_2 at $t = 0.0207$ s. Snapshots on either side of the minimum (at $t = 0.0196$ and 0.0222 s) are shown in Figure 4. At the end of the simulation ($t = 0.0251$ s), most of the spiral arm material is falling back toward the bar and is beginning to form an equatorial ring. The nascent ring is evidenced by the slender spiral arms in the last panel of Figure 4 and is easily recognized in both the low- and high-density contours in Figure 5. There are weak shocks along the outer edges of these spirals caused by the infall.

Compared to other extant polytrope simulations (such as Imamura et al. 2000), the final state ($t = 0.0251$ s) exhibits relatively more extreme structure because of the EOS. The central bar region has a stiff EOS and has the strong flattening expected close to the $m = 2$ dynamic instability point of an incompressible fluid (meridional plane eccentricity of 0.9528; Chandrasekhar 1969). On the other hand, the EOS is extremely soft in the $\rho < \rho_{\text{nuc}}$ spiral arms, with an effective polytropic index $n_{\text{eff}} > 3$ (Paper I). These regions are puffed up and have large vertical extent, as illustrated in the top panel of Figure 5. These structures are challenging to model, because they require good resolution in all three directions.

Figure 6 shows the strains h_+ and h_\times for $\theta = 0^\circ$ (an observer on the rotation axis), normalized using

$$rh_0 = \frac{G^2 M_c^2}{R_{\text{eq}} c^4} = 2174 \left(\frac{M_c}{M_\odot} \right)^2 \left(\frac{R_{\text{eq}}}{100 \text{ km}} \right)^{-1} \text{ cm}. \quad (12)$$

Here r is the distance to the fizzler. At saturation ($t \approx 0.0175$ s), the peak GW strains for an on-axis observer, for both the “+” mode and the “ \times ” mode are $h = 1.34(r/15 \text{ Mpc})^{-1} \times 10^{-22}$ with frequency 556 Hz (period 1.8 ms). Using the eigenfunctions from the linear theory, equations (5) and (6) predict peak on-axis strains of $h = 1.34(\delta\mathcal{M}/0.70)(r/15 \text{ Mpc})^{-1} \times 10^{-22}$, in remarkable agreement with the nonlinear result. For an off-axis observer, the strains for $\theta = 0^\circ, 45^\circ$, and 90° predicted by using the linear theory are in the ratios 1 : 0.813 : 0.5 and 1 : 0.797 : 0.127 for h_+ and h_\times , respectively.

Other nonlinear evolution results are consistent with results based on the linear and quasi-linear theories. During exponential growth, the P_2 and τ_g agree to within 3% (compare Tables 3 and 5); in fact, P_2 agrees to three significant figures. In Table 5, we present the nonlinear bar properties at maximum amplitude and for the final time in the simulation. The first number in each column is for the bar at maximum; the second number is for the final bar configuration. The M_b in Table 5 agrees to within two digits with that predicted by quasi-linear analysis in Table 3. The final bar results are also consistent. The final nonlinear structure and a quasi-linear structure based on equation (9) are similar in appearance and, consequently, have similar observable properties. For example, the bar radii are close, $R_{\text{bar}} = 26.6$

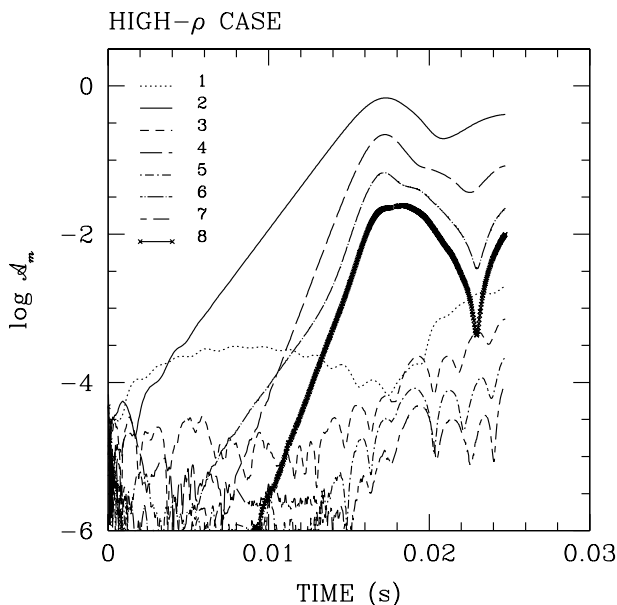


FIG. 3.—Time evolution of the global Fourier amplitudes \mathcal{A}_m for the high- ρ , $1.60 M_\odot$ nonlinear fizzler simulation. The curves show $\log(\mathcal{A}_m)$ for $m = 1\text{--}8$.

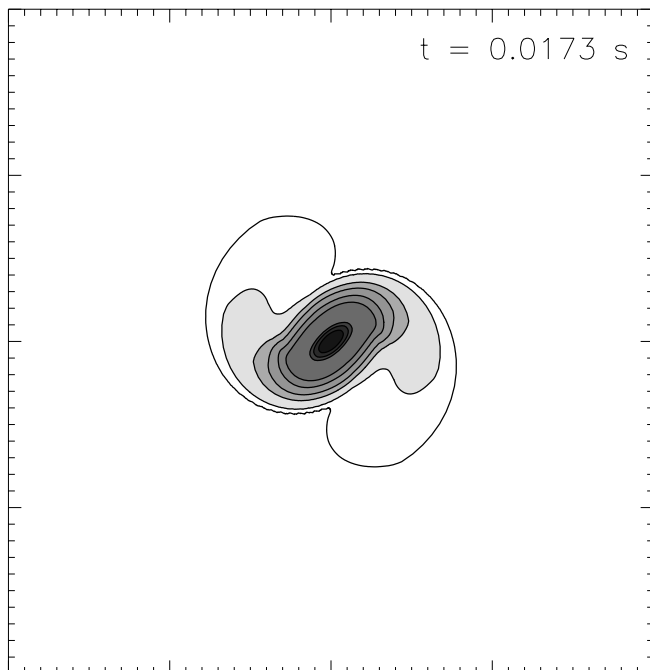


FIG. 4a

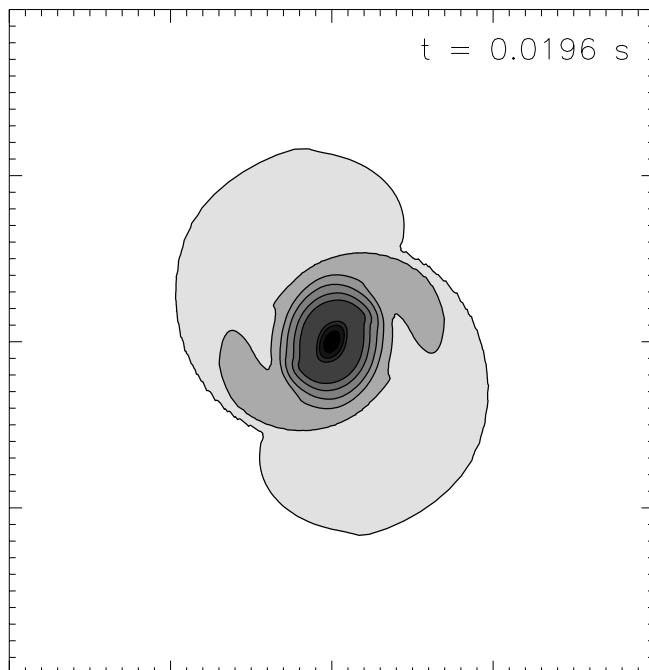


FIG. 4b

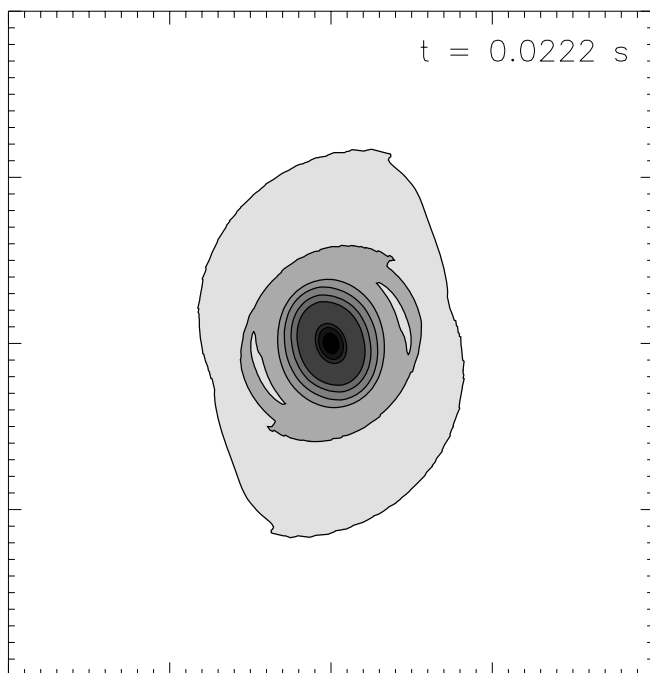


FIG. 4c

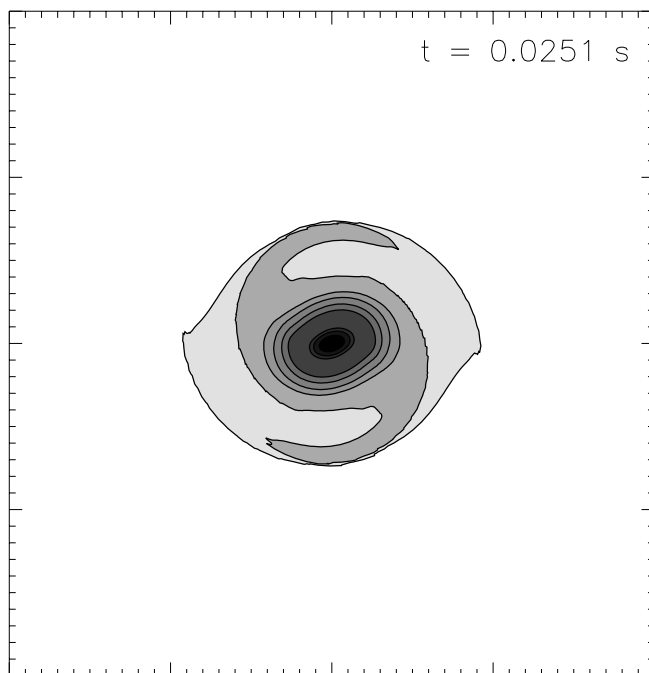


FIG. 4d

FIG. 4.—Gray-scale representations of the relative density structures in the equatorial plane for the nonlinear evolution of the high- ρ , $1.60 M_{\odot}$ fizzler shown in Fig. 3. The four images are for the times (a) $t = 0.0173$ s, (b) $t = 0.0196$ s, (c) $t = 0.0222$ s, and (d) $t = 0.0251$ s. The contours levels are normalized to ρ_c and are set to 0.0001, 0.001, 0.01, 0.03, 0.06, 0.1, 0.3, 0.6, 0.9, 0.95, 0.98, and 1.

km versus 30.4 km for the quasi-linear and nonlinear bars, respectively. At the final \mathcal{A}_2 ($\delta\mathcal{M} \approx 0.42$), the peak strain from the nonlinear simulations for an on-axis observer is $h = 8.2 (r/15 \text{ Mpc})^{-1} \times 10^{-23}$, while the linear theory for this \mathcal{A}_2 predicts $h = 7.9 (\delta\mathcal{M}/0.42) (r/15 \text{ Mpc})^{-1} \times 10^{-23}$. Note also that the final bar configuration has $M_b = 0.90M_c = 1.44 M_{\odot}$, and $J_b = 2.72 \times 10^{49} \text{ g cm}^2 \text{ s}^{-1}$.

Comparing these final bar properties to that for the $M_c = 1.42 M_{\odot}$ fizzler that sits near the bar instability threshold (Table 2, model 2b), we see that the nonlinear phase of the dynamic bar instability has driven the central object close in J_b to the angular momentum of a marginally stable axisymmetric configuration of the same mass, as predicted by Imamura et al. (2000).

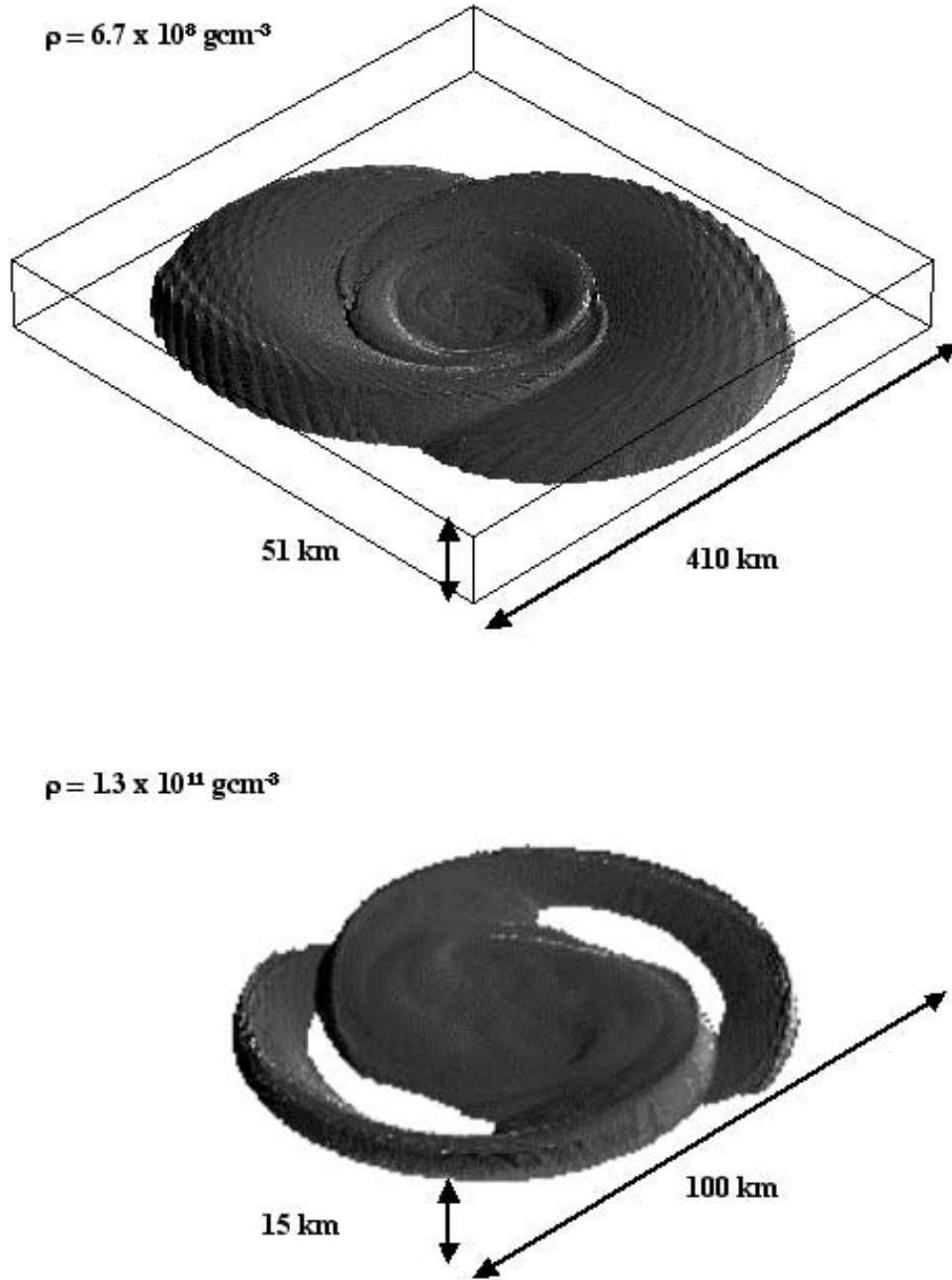


FIG. 5.—Equal density surface contours and gray-scale images for the high- ρ fizzler structures shown in Fig. 4. The upper image shows a relatively low density ($\rho = 6.7 \times 10^6 \text{ g cm}^{-3}$) to illustrate the structure of the spiral arms. Almost all the mass of the fizzler is encompassed by this contour. The bottom contour is designed to show the high-density material ($\rho \geq 1.3 \times 10^{13} \text{ g cm}^{-3}$) in and near the central bar. At this point in the evolution, the outer spiral arms are falling in to form a ring around the central bar. The fine patterning in the images is an artifact of the contouring software we are using.

3.2.4. Nonlinear Simulation of a Low- ρ Fizzler

Consider the $1.58 M_{\odot}$ fizzler with $J = 4.97 \times 10^{49} \text{ g cm}^2 \text{ s}^{-1}$ (model 1b). Initially, as shown in Table 1, for $Y_e \approx 0.32$, this fizzler has ρ_c less than ρ_{nuc} and $T/|W|$ below the bar mode dynamic stability limit. The $\langle \tau_{\text{de}} \rangle$ is tenths of a second, and so the fizzler deleptonizes and spins up to dynamic instability in the bar mode. The dynamically unstable fizzler (model 1b) chosen for simulation is the next to last model of the top deleptonization sequence in Table 1. The properties of the deleptonized equilibrium fizzler are given in Tables 1 and 2, and its structure is shown in Figure 7. The barlike

mode was unstable and the $m = 3$ mode stable in the linear regime. The oscillation period and growth time for the bar mode were $P_2 = 5.78 \text{ ms}$ and $\tau_g = 7.36 \text{ ms}$, respectively. For model 1b, $\delta \mathcal{M} = 1.17 \mathcal{A}_2$. The peak GW strain amplitudes for an on-axis observer were $h = 5.4 \delta \mathcal{M} (r/15 \text{ Mpc})^{-1} \times 10^{-23}$ with wave frequency 175 Hz. For an off-axis observer, the strains for $\theta = 0^\circ$, 45° , and 90° are in the ratios $1 : 0.83 : 0.5$ and $1 : 0.82 : 0.159$ for h_+ and h_{\times} , respectively.

We show the low-order global Fourier amplitudes for the density perturbations and the strains h_+ and h_{\times} for $\theta = 0^\circ$ in Figures 8 and 9, respectively. The strains in Figure 9 are normalized using equation (12). After the initial organizational

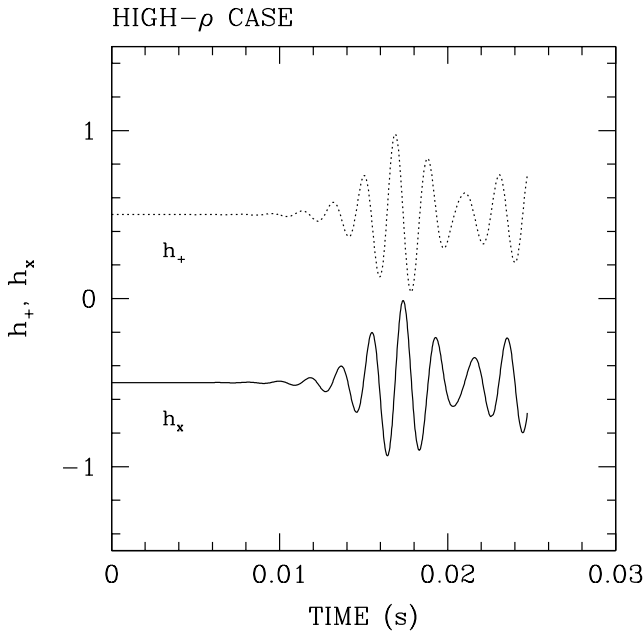


FIG. 6.—Time evolution of the strains h_+ and h_x for the high- ρ , $1.60 M_\odot$ nonlinear fizzler simulation (see Fig. 3) for $\theta = 0^\circ$. The h -values are in units of $(G^2 M_c^2)/(r R_{\text{eq}} c^4) = (12, 620 \text{ cm})/r$.

period, the bar grew exponentially. When $\mathcal{A}_2 \ll 1$, the bar grew with $\tau_g = 8.1 \text{ ms}$ and $P_{2,l} = 5.6 \text{ ms}$, in good agreement with the linear analysis. After \mathcal{A}_2 passed 0.2–0.3, the central region started to shed angular momentum to the outer arm region ending the linear growth phase. Growth saturated around $\mathcal{A}_2 = 0.44$ ($\delta\mathcal{M} \approx 0.51$) with bar mass $M_b = 0.80 M_c$. At saturation, the peak GW strains for an on-axis observer are $h = 2.78(r/15 \text{ Mpc})^{-1} \times 10^{-23}$ with frequency 179 Hz (period $P_{2,l} = 5.6 \text{ ms}$). The linear theory predicts peak strains of $h = 2.74(\delta\mathcal{M}/0.51)(r/15 \text{ Mpc})^{-1} \times 10^{-23}$, again, in remarkable agreement with the nonlinear result.

After saturation, the even $m > 2$ components decayed, and the overall bar amplitude decayed slowly. Around 83.4 ms, the \mathcal{A}_2 “glitched” followed by high-speed oscillations. The “glitch” is understood as follows. Initially, $\rho_c < \rho_{\text{nuc}}$. As the bar shed J , it contracted and compressed (Imamura et al. 2000). Around 83.4 ms, ρ_c reached ρ_{nuc} , and the EOS in the core region stiffened. This led to a dynamical adjustment of the structure of the fizzler and the *ringing*. There was a clear change in the oscillation frequency after 83.4 ms. The oscillation period at the end of the nonlinear simulation was $P_{2,f} = 4.2 \text{ ms}$.

The long-term nonlinear results agree less well with the quasi-linear theory. However, the prediction of Imamura et al. (2000) that the bar instability drives the central object to the marginally stable state still holds up. Compare model 1b in Table 5 to model 1c in Table 2. The agreement between

the quasi-linear and nonlinear simulations breaks down for other comparisons. The final nonlinear and quasi-linear bar structures are similar in appearance, but there are differences in detail. The bar radii are reasonably close, $R_{\text{bar}} = 51.7 \text{ km}$ versus 56.1 km (model 1b) for the quasi-linear bar and the nonlinear bar, respectively; however, the linear GW results are in poor agreement with the nonlinear simulation. At the final \mathcal{A}_2 ($\delta\mathcal{M} \approx 0.29$), the peak strain from the nonlinear simulation for an on-axis observer is $h = 2.24(r/15 \text{ Mpc})^{-1} \times 10^{-23}$. The linear torque for model 1b has strain $h = 1.72(\delta\mathcal{M}/0.29)(r/15 \text{ Mpc})^{-1} \times 10^{-23}$. The agreement is worse if model 1c is used for the comparison. The more compressible fizzler is less accurately modeled by our linear theory than the stiff fizzler.

4. DISCUSSION

4.1. Detectability of GW Emission by Fizzlers

Currently, there are several Earth-bound, kilometer-baseline, broadband gravitational wave detectors coming on-line or in the developmental stages. These include the LIGO project (Abramovici et al. 1992), the VIRGO project (Bradaschia et al. 1990), the GEO-600 project (Danzmann et al. 1995), and the TAMA project (Tsubono et al. 1997). All of these experiments utilize Michelson laser interferometers for the detection of GWs. Here for illustrative purposes, we consider fizzlers as possible targets for LIGO. The LIGO design specification sensitivity levels over the frequency range 100–1000 Hz are 3×10^{-23} to 10^{-22} per $\text{Hz}^{-1/2}$ (Lazzarini & Weiss 1996; B. Barish 2002, private communication; see Fig. 10).

Our modeled fizzlers have $f = 60\text{--}600 \text{ Hz}$ with rms strains of about 2×10^{-23} (low- ρ fizzler) to 2×10^{-22} (high- ρ fizzler) for $r = 15 \text{ Mpc}$. So, if the search resolution is about 1 Hz, in other words, if the fizzlers persist for hundreds of cycles, then fizzlers located at Virgo distances fall near the LIGO design detection threshold, especially fizzlers that reach dynamic instability just above the neutron star density regime. We have followed our nonlinear bars for only about 5–10 wave cycles. Over these times, the fizzler bars are strong enough to be detected by LIGO I as burst sources only if they are within the Local Group of galaxies. This is a useful start, but fizzlers are not likely to occur at a significant rate over such a small volume. An understanding of the long-term evolution of fizzler bars is thus critical for knowing whether fizzlers are viable targets for LIGO over more interesting distances. Unfortunately, the long-term evolution of rotating fluid bars is a complex and problematic subject.

Fryer et al. (2002) recently estimated the GW emission from bar mode unstable proto-neutron stars. Under the assumption that mass enclosed within a bar mode unstable core went into the bar mode, they find strains as large as 10^{-22} for $f \sim 1000 \text{ Hz}$ and $r = 10 \text{ Mpc}$ (see Fryer et al.

TABLE 5
BAR PROPERTIES: NONLINEAR RESULTS

Model	$P_{2,l}$ (ms)	τ_g (ms)	$P_{2,f}$ (ms)	M_b/M_c	R_b (km)	J_b ($\text{g cm}^2 \text{ s}^{-1}$)	\mathcal{A}_2
1b.....	5.6	8.1	2.94	0.80	56.1, 52.9	$2.83 \times 10^{49}, 2.62 \times 10^{49}$	0.44, 0.27
2a.....	1.82	1.32	1.80	0.90	32.8, 30.4	$2.71 \times 10^{49}, 2.72 \times 10^{49}$	0.69, 0.41

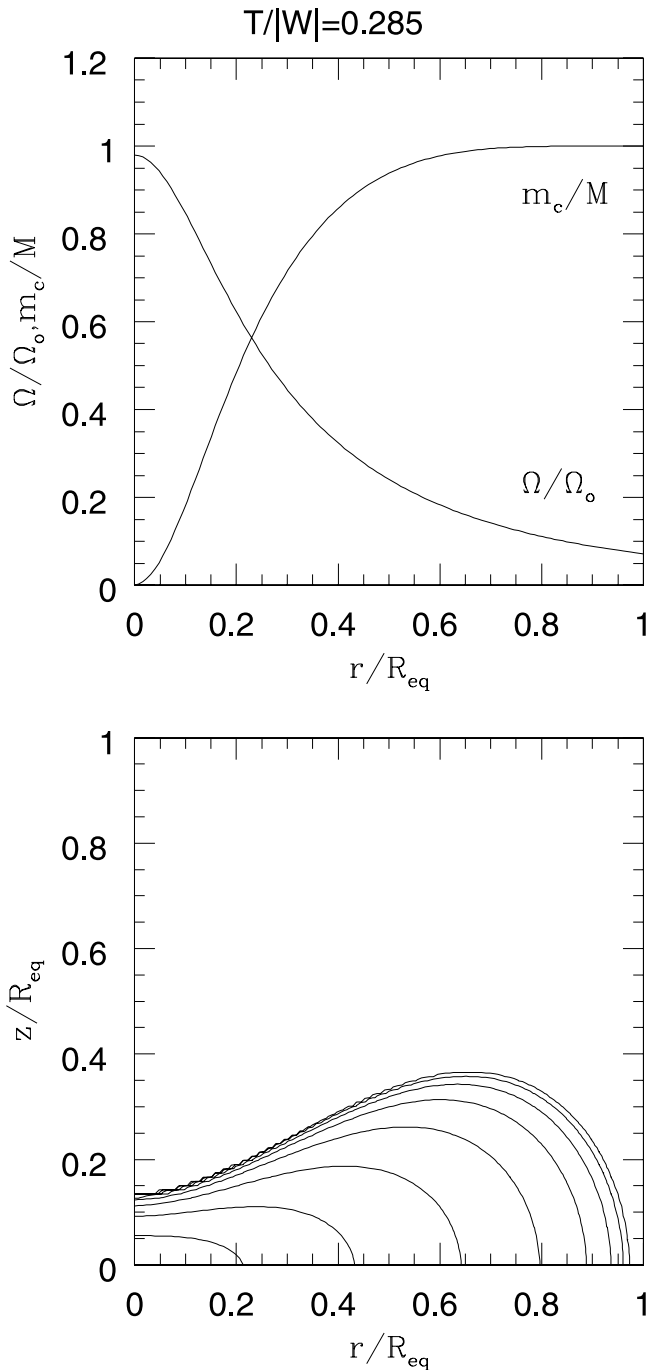


FIG. 7.—Equilibrium density structure and $\Omega(\varpi)$ and $m_c(\varpi)$ distributions for a $1.58 M_\odot$ fizzler calculated for the Maclaurin spheroid angular momentum distribution and EOS parameters $Y_e = 0.23$, $S_b = 1.5$ k, and $K = 180$ MeV. The model is just beyond the dynamic stability limit with $\rho_c = 5.62 \times 10^{13}$ g cm $^{-3}$, $J = 4.98 \times 10^{49}$ g cm 2 s $^{-1}$, and $T/|W| = 0.285$. The contour levels are set to $\rho/\rho_c = 0.9, 0.1, 0.01, 0.001, 10^{-4}, 10^{-5}, 10^{-6}$, and 10^{-7} . The fizzler has a central $\Omega_0 = 1088$ rad s $^{-1}$.

2002, Table 1 and Fig. 7). These limits are similar to the strains we find for high- ρ fizzlers, that is, for fizzlers near nuclear density.

The waveforms we find in our nonlinear simulations (Figs. 6 and 9) differ from those found by Houser (1998) for stiff polytropes. Houser’s curves (her Fig. 16) look mostly like damped oscillators with a steady decline from peak amplitude. Our Figure 6 shows a marked oscillation in

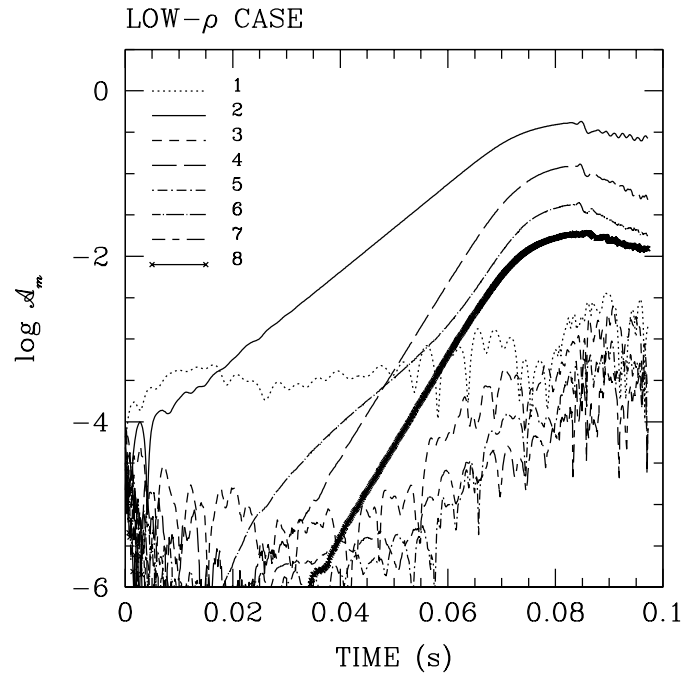


FIG. 8.—Time evolution of the global Fourier amplitudes \mathcal{A}_m for the low- ρ , $1.58 M_\odot$ nonlinear fizzler simulation. The curves show $\log(\mathcal{A}_m)$ for $m = 1-8$.

amplitude that roughly mimics the \mathcal{A}_2 variations. Figure 9 is less clear-cut. We plan to do longer nonlinear integrations of fizzlers and will be attentive to better characterizing their waveform signature. It is unclear at present whether these differences have to do with differences in EOS or numerical techniques.

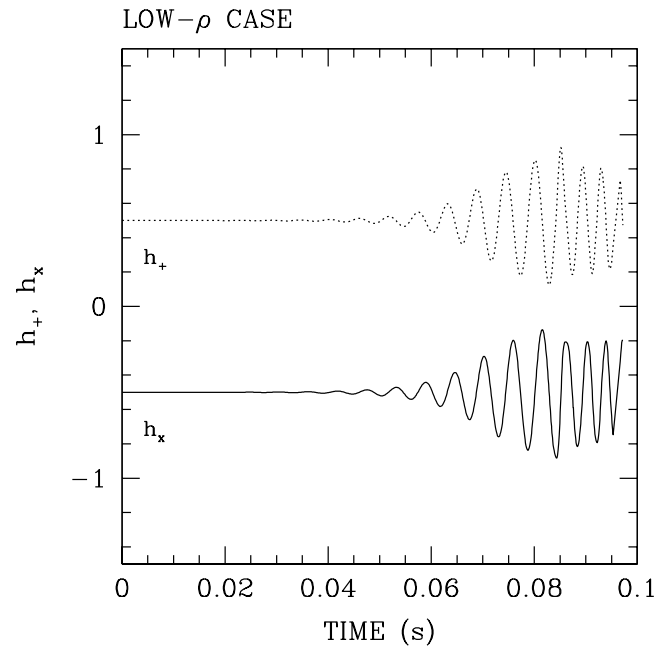


FIG. 9.—Time evolution of the strains h_+ and h_x for the low- ρ , $1.58 M_\odot$ nonlinear fizzler simulations (see Fig. 6) for $\theta = 0^\circ$. The h -values are in units of $(G^2 M_c^2)/(r R_{\text{eq}} c^4) = (3413 \text{ cm})/r$.

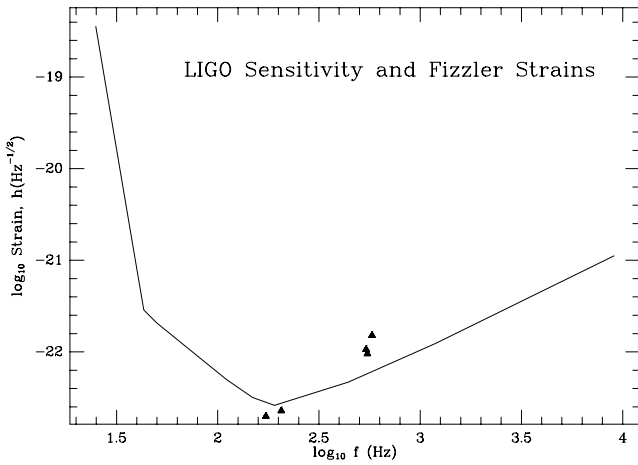


FIG. 10.—Design specifications for the LIGO sensitivity levels (Lazzarini & Weiss 1996; B. Barish 2002, private communication). Plotted as triangles are the fizzler strains h_+ for an on-axis observer as given for a selection of fizzler models in Table 4. For off-axis observers, the strains are smaller, by factors of up to 2–8 depending on the polarization of the wave. The strains are normalized using $\delta M = 0.70$ and 0.51 for the high-frequency and low-frequency fizzlers, respectively. Fizzlers at Virgo distances are just at the limit of LIGO sensitivity if the search bandwidth is ~ 1 Hz.

4.2. Long-Term Evolution of the Bar

At the end of our two nonlinear simulations, the bars resemble Dedekind-like S-type Riemann ellipsoids; i.e., they are fluid bars whose surfaces tumble more slowly than the fluid circulates within the bars (Chandrasekhar 1969; Durisen & Tohline 1985; Cazes & Tohline 2000). They have J_b approximately equal to the angular momentum J_{dyn} of an axisymmetric fizzler with $M = M_b$, which is marginally stable to dynamic barlike instabilities ($T/|W| \approx 0.26\text{--}0.27$, depending upon ρ_c). The J_b values are greater, however, than the angular momentum J_{sec} of the axisymmetric fizzler with M_b , which is marginally stable to the secular instability ($T/|W| \approx 0.14$). This means that, in principle, the post-dynamic instability fizzler bars can maintain their triaxial shapes in the absence of dissipation. The long-term evolution of the bar is then driven by mechanisms that remove angular momentum or dissipate energy, such as the emission of GW radiation, Newtonian torques, shock heating, bulk viscosity, and deleptonization and cooling of the hot, lepton-rich material. The Newtonian torque referred to here arises because of the gravitational coupling between the central bar and the ring or disk of material ejected in the instability. The timescales for GW radiation, Newtonian torques, and deleptonization are all much longer than the dynamic timescale for the bar, and this means rather long evolutions are required using explicit hydrodynamics techniques. Numerical resolution becomes a problem in the case of fizzlers, because the EOS is extremely compressible (see Paper I, Fig. 1).

In what directions will different mechanisms drive the bars? Newtonian torques will tend to reduce J_b to J_{sec} and so will ultimately tend to drive the fizzler toward a rotating axisymmetric state that is both secularly and dynamically stable to barlike distortions (Imamura et al. 2000; Imamura & Durisen 2001). For GRR, the evolution can initially be toward a Dedekind (zero surface rotation) bar structure (Detweiler & Lindblom 1977), but the combination of Newtonian and GRR torques probably tend to the axisymmetric state, because Newtonian coupling to the ejecta should prevent zero surface rotation. Deleptonization and cooling, on the other hand, drive the EOS toward a young neutron star EOS. All of these processes will induce contraction of the bar, which should tend to amplify its distortion. Shocks may occur near the ends of the bar whenever it achieves a large enough amplitude that sharp turns at supersonic motions are required in the circulating fluid (Cazes & Tohline 2000). Both bulk viscosity and heating by shocks tend to decrease the bar amplitude (Houser et al. 1994; Durisen et al. 2001).

Determining precisely how the above processes interact is beyond the scope of the present work, even ignoring the possibility of further infall from the surrounding star. However, we can estimate the properties for the final deleptonized, axisymmetric, marginally stable end-state fizzler. We assume, for simplicity, that deleptonization and cooling are complete and use the cold β -equilibrium EOS (Canuto 1974). Then the ultimate end states for bar evolution ($T/|W| \approx 0.14$ models) for the two simulations discussed in detail in § 3 have $J_{\text{sec}} = 9.51 \times 10^{48}$ and 1.23×10^{49} g cm² s⁻¹, respectively (see Table 6). Both bars must dispose of roughly the same amount of angular momentum, $\Delta J = J_{\text{dyn}} - J_{\text{sec}} = 1.73 \times 10^{49}$ and 1.33×10^{49} g cm² s⁻¹, respectively. This is ample angular momentum for both bars to radiate GW radiation for 1000 cycles at amplitudes sufficient for LIGO I to detect. Once f -mode secular stability is achieved, the r -mode instabilities may remove considerable additional angular momentum at very low GW strains over a much longer timescale (see § 2.4).

The issue then becomes how much of this angular momentum is shed through GW radiation. The bar is surrounded by the material ejected in spiral arms during the early phases of dynamic bar instability. If the Newtonian torque and GRR torque maintain a similar relative strength during a long postinstability bar evolution, then most of the angular momentum will be used to push the material ejected in the spiral arms away from the bar. GW emission will then not be dynamically important. Whether it will be sufficient for LIGO detection depends on the how quickly Newtonian torques drain angular momentum and what this does to the bar amplitude.

An extensive study of dynamic barlike mode instabilities in $n = 3/2$ polytropes carried out by Durisen et al. (2001) illustrates the sensitivity of bar persistence to the treatment

TABLE 6
POSSIBLE FIZZLER END STATES

Model	M_b (M_\odot)	J_b (g cm ² s ⁻¹)	ρ_b (g cm ⁻³)	J_{sec} (g cm ² s ⁻¹)	ρ_{sec} (g cm ⁻³)
1b.....	1.19	2.68×10^{49}	5.62×10^{13}	9.51×10^{48}	6.92×10^{14}
2a.....	1.43	2.57×10^{49}	2.24×10^{14}	1.23×10^{49}	7.59×10^{14}

of dissipative mechanisms. They showed that, with no heating by shear or bulk viscosity, the bar lasts for many cycles at about the \mathcal{A}_2 amplitude reached after rebound from the first minimum (see Fig. 3). If heating by artificial bulk viscosity in shocks is included, the central bar dissipates, leaving an axisymmetric central object surrounded by a disk as the end state. This was first shown by Houser et al. (1994). The calculation without artificial viscosity used a strict polytropic equation of state, equivalent to assuming precisely isentropic evolution. But shocks do form when the initially expanding spiral arms fall back. So, keeping the entropy per gram constant effectively causes loss of energy behind the shocks. The simulations that include heating by artificial viscosity conserve total energy. The difference is only about 10% of the total energy, yet it makes the critical difference between whether the bar persists or not! The full physics of the fizzler problem needs to be considered to determine the fate of the bar.

Finally, we have ignored here the possibility of an accretion disk forming around the fizzler. The relative amount of mass shed to the ring increases with the $T/|W|$ of the unstable fizzler. The increase is larger for fizzlers with more compressible EOSs. For fizzlers with $Y_e = 0.23\text{--}0.25$, the disk mass ranged from 6% to 24% for $T/|W| = 0.255\text{--}0.285$. For fizzlers with $Y_e = 0.15$, the disk mass ranged from 7% to 10% for the same range in $T/|W|$. If the bar persists, accretion is unlikely because Newtonian torques alone are effective at repelling the circumbar material (e.g., Durisen et al. 1986). However, accretion may become an additional complication when or if the bar amplitude damps. It is even possible that exotic bound objects, such as neutron star planets, might form by gravitational instabilities (e.g., Boss 2001; Durisen et al. 2001) in the strongly cooling and deleptonizing circumfizzler disk.

4.3. Rotating Core Collapse and Supernovae

So far, we have concerned ourselves only with the evolution of the fizzler itself. Another question of considerable interest is the fate of the rest of the star. Will fizzler formation completely abort supernova formation or just weaken and/or delay it? Observationally, a clue to this possibility lies in the power and waveform of the GW emission from a fizzler compared to those of proto-neutron stars. Comparing the strain amplitudes (Fig. 10) and the waveforms (Figs. 6 and 9) for the low- ρ and high- ρ models, we get a feel for the difference between direct proto-neutron star formation and fizzler formation. The low- ρ case, the fizzler case, has lower strain amplitude and lower radiation frequency. An interesting effect occurs as the bar mode unstable fizzler radiates GW. The energy and angular momentum loss causes the bar to contract and spin up, and the strain amplitude increases. Furthermore, after the central density of the bar exceeds nuclear density, the EOS stiffens and the frequency of the GW emission abruptly increases. The increase in the GW emission is not expected if a proto-neutron star forms.

Theoretically, a complete answer to the question requires detailed collapse calculations with rotation. However, a basic issue is whether the released gravitational energy is large enough to power a supernova event. The gravitational binding energies for the envelopes of 10–40 M_\odot stars are $|W_{b,e}| = 10^{50}$ to 3×10^{51} ergs (e.g., Burrows & Young 2000). In the most optimistic scenario, a Type II SN out-

burst is possible if the gravitational binding energy of the fizzler exceeds $|W_{b,e}|$. On the basis of our equilibrium fizzler calculations, even for the conservative assumption that the initial fizzlers have maximum $Y_e = 0.4$, we find that fizzlers have $|W| > 7 \times 10^{51}$ ergs for $\rho_c > 10^{11}$ g cm $^{-3}$, sufficient to unbind even the envelopes of 40 M_\odot stars. Fizzlers have sufficient energy available to cause SN outbursts.

The question is then how much of $|W|$ and how quickly it is converted into bulk kinetic energy by the rebound shock. This is a difficult question because the physics of core collapse and shock generation in a rotating massive star is complex—simulations including multidimensional convection and neutrino transport for a hot nuclear EOS must be performed. Recent progress on this difficult problem has been made by Fryer & Heger (2000), who studied core collapse in one of the rotating massive main-sequence star models evolved by Heger et al. (2000). Fryer & Heger used model E15B of Heger, Langer, & Woosley, which had iron core mass $M_c = 1.40 M_\odot$ and $J_c = 4.07 \times 10^{49}$ g cm 2 s $^{-1}$. Fryer & Heger found that the collapsing core reached nearly the same ρ_c as a corresponding nonrotating core; a fizzler did not form. The bounce, however, was delayed and less violent and had more fallback when compared to a nonrotating core collapse. Although the case studied by Fryer & Heger led to an SN outburst, it is not clear yet whether true fizzlers do.

The Fryer & Heger (2000) collapse reached nuclear density, that is, it did not lead to fizzler formation despite the fact that it had large J_c . If model E15B had specific angular momentum distribution similar to that of a Maclaurin spheroid, then for its combination of M_c and J_c , we would predict that the resultant collapse would have been well within the fizzler regime. Fryer & Heger's result is understandable, however, because the core model used by Fryer & Heger had an angular momentum distribution that concentrated much more angular momentum toward the equatorial region of the core than would a Maclaurin spheroid specific angular momentum distribution. Consequently, the collapse was less inhibited by rotation in the central region and thus reached higher density at bounce. The angular momentum distribution in the massive stellar core prior to collapse plays a major role in determining whether a fizzler forms or does not form. This is problematic, because even close to the main sequence, the angular momentum distribution in the cores of massive stars is not well understood (Deupree 2001). In other words, a key parameter that determines the true diversity of core collapse outcomes is poorly known.

5. SUMMARY

In this paper, we have studied the evolution of fizzlers due to deleptonization. These rapidly rotating, aborted stellar core collapses evolve quasi-statically until they become dynamically unstable to barlike modes. We have, for the first time, performed nonlinear three-dimensional hydrodynamic simulations of these unstable objects with a realistic fizzler EOS, and we have computed the resultant GW emission during the early nonlinear phases. The nonlinear behavior of the dynamic barlike instability in fizzlers is qualitatively similar to that found for polytropes, in that the evolution is limited and controlled by the Newtonian gravitational self-interaction torque, not by the gravitational radiation reaction torque. This is true even for fizzlers that reach dynamic instability at close to nuclear density.

Although determination of the detailed development of the dynamic barlike instability and the GW emission waveform requires nonlinear simulations, we find that many important global properties of the unstable fizzlers may be understood using linear and quasi-linear techniques alone, including the order of magnitude of the rms GW strains.

We find that even for the most compact, high- ρ fizzlers, the bars are only weak sources of GW emission and produce strains of $r_{15}h = 10^{-23}$ to 10^{-22} with frequencies of 60–600 Hz. Fizzler bars that last for no more than about 10 cycles will be visible by LIGO I as *burst* sources only if they occur in the Local Group of galaxies. If the bars manage to persist for hundreds of GW cycles, however, fizzlers may be detectable by LIGO I to Virgo distances. The crucial question is

whether the tumbling bars formed by fizzlers persist at high amplitude for hundreds of GW cycles. This can only be answered by longer simulations that include more of the relevant physics. We have preparations for such simulations underway.

We would like to thank M. Bate, L. Lindblom, K. New, and J. E. Tohline for useful conversations about aspects of this problem and A. C. Mejia for assistance in the generation of some of the figures for this manuscript. Large amounts of computing time were made available for this project by Indiana University’s University Information Technology Services and the National Center for Supercomputing Applications.

REFERENCES

- Abramovici, A., et al. 1995, in Proc. 1994 Snowmass Summer Study on Particle and Nuclear Astrophysics and Cosmology in the Next Millennium, ed. E. W. Kolb & R. Peccei (Singapore: World Scientific), 398
- Andersson, N. 1998, ApJ, 502, 708
- Bate, M. R. 1998, ApJ, 508, L95
- Bonazzola, S., Frieben, J., &ourgoulhon, E. 1996, ApJ, 460, 379
- . 1998, A&A, 331, 280
- Boss, A. P. 2001, ApJ, 563, 367
- Bowers, R., & Deeming, T. 1984, Astrophysics I, Stars (Boston: Jones & Bartlett)
- Bradaschia, C., et al. 1990, Nucl. Instrum. Methods Phys. A, 289, 518
- Burrows, A., Mazurek, T. J., & Lattimer, J. M. 1981, ApJ, 251, 325
- Burrows, A., & Young, T. 2000, Phys. Rep., 333, 63
- Canuto, V. 1974, ARA&A, 12, 167
- Cazes, J. E., & Tohline, J. E. 2000, ApJ, 532, 1051
- Chandrasekhar, S. 1969, Ellipsoidal Figures of Equilibrium (New Haven: Yale Univ. Press)
- Danzmann, K., et al. 1995, in Proc. of the First Eduardo Amaldi Conf. on Gravitational Wave Experiments, ed. E. Coccia, G. Pizella, & F. Ronga (Singapore: World Scientific), 100
- Detweiler, S., & Lindblom, L. 1977, ApJ, 213, 193
- Deupree, R. G. 2001, ApJ, 552, 268
- Durisen, R. H., Gingold, R. A., Tohline, J. E., & Boss, A. P. 1986, ApJ, 305, 281
- Durisen, R. H., Pickett, B. K., Bate, M. R., Imamura, J. N., Brandt, A., & Sterzik, M. F. 2001, in IAU Symp. 200, The Formation of Binary Stars, ed. H. Zinneker & R. Mathieu (Dordrecht: Kluwer), 381
- Durisen, R. H., & Tohline, J. E. 1985, in Protostars and Planets II, ed. D. C. Black & M. S. Matthews (Tucson: Univ. Arizona Press), 534
- Finn, L. S., & Evans, C. R. 1990, ApJ, 351, 588
- Friedman, J. L., & Morsink, S. M. 1998, ApJ, 502, 714
- Friedman, J. L., & Schutz, B. F. 1978, ApJ, 222, 281
- Fryer, C. L., & Heger, A. 2000, ApJ, 541, 1033
- Fryer, C. L., Holz, D. E., & Hughes, S. A. 2002, ApJ, 565, 430
- Hachisu, I. 1986, ApJS, 61, 479
- Hashimoto, M. 1995, Prog. Theor. Phys., 94, 663
- Hayashi, A., Eriguchi, Y., & Hashimoto, M. 1998, ApJ, 492, 286
- . 1999, ApJ, 521, 376
- Heger, A., Langer, N., & Woosley, S. E. 2000, ApJ, 528, 368
- Houser, J. L. 1998, MNRAS, 299, 1069
- Houser, J. L., Centrella, J. M., & Smith, S. 1994, Phys. Rev. Lett., 72, 1314
- Imamura, J. M., & Durisen, R. H. 2001, ApJ, 549, 1062
- Imamura, J. N., Durisen, R. H., & Pickett, B. K. 2000, ApJ, 528, 946
- Imamura, J. N., Toman, J., Durisen, R. H., Pickett, B. K., & Yang, S. 1995, ApJ, 444, 363
- Lattimer, J., & Swesty, D. 1991, Nucl. Phys. A, 535, 331
- Lazzarini, A., & Weiss, R. 1996, LIGO Science Requirements Document (Caltech: LIGO Group)
- Lebovitz, N. R. 1972, ApJ, 175, 171
- Lindblom, L., & Detweiler, S. 1977, ApJ, 211, 565
- Lindblom, L., Owen, B., & Morsink, S. M. 1998, Phys. Rev. Lett., 80, 4843
- Lindblom, L., Tohline, J. E., & Vallisneri, M. 2001, Phys. Rev. Lett., 86, 152
- Mezzacappa, A., & Bruenn, S. W. 1993, ApJ, 405, 637
- New, K. C. B., Centrella, J., & Tohline, J. E. 2000, Phys. Rev. D, 62, 4019
- Pickett, B. K., Durisen, R. H., & Davis, G. A. 1996, ApJ, 458, 714
- Rampp, M., Müller, E., & Ruffert, M. 1998, A&A, 332, 969
- Shapiro, S. L., & Lightman, A. P. 1976, ApJ, 207, 263
- Shibata, M., Baumgarte, T. W., & Shapiro, S. L. 2000, ApJ, 542, 453
- Smith, S. C., Houser, J. L., & Centrella, J. M. 1996, ApJ, 458, 236
- Stergioulas, N., & Font, J. A. 2001, Phys. Rev. Lett., 86, 1148
- Stergioulas, N., & Friedman, J. L. 1998, ApJ, 492, 301
- Strobel, K., Schaab, C., & Weigel, M. K. 1999, A&A, 350, 497
- Tassoul, J.-L. 1978, Theory of Rotating Stars (Princeton: Princeton Univ. Press)
- Timmes, F. X., Woosely, S. E., & Weaver, T. A. 1996, ApJ, 457, 834
- Tohline, J. E., & Durisen, R. H. 2001, in IAU Symp. 200, The Formation of Binary Stars, ed. B. Reipurth & H. Zinneker (Dordrecht: Kluwer), 40
- Tohline, J. E., Durisen, R. H., & McCollough, M. 1985, ApJ, 298, 220
- Toman, J., Imamura, J. N., Pickett, B. K., & Durisen, R. H. 1998, ApJ, 497, 370
- Tsubono, K., et al. 1997, in Frontiers Science Ser. 20, Gravitational Wave Detection, ed. K. Tsubono, N. M. K. Fujimoto, & K. Kuroda (Tokyo: Universal Academy), 183
- Yoshida, S., & Eriguchi, Y. 1995, ApJ, 438, 830
- . 1997, ApJ, 490, 779
- . 1999, ApJ, 515, 414
- Yoshida, S., Rezzolla, L., Karino, S., & Eriguchi, Y. 2002, ApJ, 568, L41
- Zwinger, T., & Müller, E. 1997, A&A, 320, 209